

Compton scattering—for example, in a corona above the disk<sup>1,4,11</sup>—is not affected as much. According to this picture, the time delay between the X-ray dip and the appearance of the superluminal knot corresponds to the travel time of the disturbance from the inner accretion disk to the core of the radio jet.

Another property shared by 3C120 and GRS1915+105 is the bulk velocity of the jet needed to explain the apparent superluminal motion: 0.98c in each case (Lorentz factor  $\approx 5$ )<sup>6,20</sup>. The one-sided observed jet in 3C120 contrasts with the two oppositely directed jets in the microquasar. This can readily be explained as a consequence of the stronger relativistic beaming of the approaching jet in 3C120, because the angle between the jet and the line of sight is smaller ( $<20^\circ$  compared with  $66^\circ$  in GRS1915+105)<sup>6,20</sup>.

The radio galaxy 3C120 is therefore similar to a scaled-up version of a microquasar. It may be possible to adapt models for the closer microquasars—whose accretion processes are better studied owing to higher and more rapidly variable X-ray fluxes—to their distant AGN cousins. We expect the scaling factor to be proportional to the radius of the innermost orbit around the black hole<sup>3</sup>, which ranges from  $3R_S$  for a static black hole to  $0.5R_S$  for the maximally rotating case<sup>21</sup>. Here,  $R_S \propto M$  is the Schwarzschild radius, with the mass of the black hole  $M = 1.6\text{--}5.1 \times 10^7$  solar masses in 3C120 (ref. 22) and 10–14 solar masses in GRS1915+105 (ref. 2). The distance of the core of the radio jet to the black hole is about  $7 \times 10^4$  times higher in 3C120 than in GRS1915+105 (ref. 20), whereas the time interval between X-ray dips is about  $5 \times 10^5$  times longer (0.5–1.2 yr for 3C120 versus 25–100 s for the microquasar<sup>4</sup>). These values are, respectively, 20–70 and 2–10 times lower than the ratio of black hole masses. The factor of 2–10 is small compared to the uncertainties in our theoretical understanding of how the time between events relates to the physical parameters of the accretion disk. The greater discrepancy in the ratio of length scales implies that the conditions governing formation of the radio core—perhaps the pressure of the external medium or the magnetic field in the jet—are different in the two objects. □

Received 15 January; accepted 26 April 2002; doi:10.1038/nature00772.

1. Mirabel, I. F. & Rodríguez, L. F. Microquasars in our Galaxy. *Nature* **392**, 673–676 (1998).
2. Greiner, J., Cuby, J. G. & McCaughrean, M. J. An unusually massive stellar black hole in the Galaxy. *Nature* **414**, 522–525 (2001).
3. Meier, D. L., Koide, S. & Uchida, Y. Magnetohydrodynamic production of relativistic jets. *Science* **291**, 84–92 (2000).
4. Belloni, T. Inner disk oscillations. *Astrophys. Space Sci.* **276** (suppl.), 145–152 (2001).
5. Gómez, J. L., Martí, J. M., Marscher, A. P., Ibáñez, J. M. & Alberdi, A. Hydrodynamical models of superluminal sources. *Astrophys. J.* **482**, L33–L36 (1997).
6. Gómez, J. L., Marscher, A. P., Alberdi, A., Jorstad, S. G. & García-Miró, C. Flashing superluminal components in the jet of the radio galaxy 3C120. *Science* **289**, 2317–2320 (2000).
7. Gómez, J. L., Marscher, A. P., Alberdi, A., Jorstad, S. G. & Agudo, I. Monthly 43 GHz VLBA polarimetric monitoring of 3C 120 over 16 epochs: evidence for trailing shocks in a relativistic jet. *Astrophys. J.* **561**, L161–L164 (2001).
8. Grandi, P. et al. ROSAT, ASCA, and OSSE observations of the broad-line radio galaxy 3C 120. *Astrophys. J.* **487**, 636–643 (1997).
9. Halpern, J. P. X-ray spectrum and variability of 3C 120. *Astrophys. J.* **290**, 130–135 (1985).
10. Maraschi, L. et al. Coordinated X-ray, ultraviolet, and optical observations of 3C 120. *Astrophys. J.* **368**, 138–151 (1991).
11. Zdziarski, A. & Grandi, P. The broadband spectrum of 3C 120 observed by BeppoSAX. *Astrophys. J.* **551**, 186–196 (2001).
12. Mann, H. B. & Whitney, D. R. On a test of whether one of two random variables is stochastically larger than the other. *Ann. Math. Stat.* **18**, 50–60 (1947).
13. Shapiro, S. S. & Wilk, M. B. An analysis of variance test for normality (complete samples). *Biometrika* **52**, 591–611 (1965).
14. Feller, W. *An Introduction to Probability Theory and its Applications*, 2nd edn 322 (Wiley, New York, 1968).
15. Klein-Wolt, M. et al. Hard X-ray states and radio emission in GRS 1915+105. *Mon. Not. R. Astron. Soc.* **331**, 745–764 (2002).
16. Marscher, A. P. Relativistic jets and the continuum emission in QSOs. *Astrophys. J.* **235**, 386–391 (1980).
17. Reynolds, S. P. Theoretical studies of compact radio sources. I. Synchrotron radiation from relativistic flows. *Astrophys. J.* **256**, 13–27 (1982).
18. Junor, W., Biretta, J. A. & Livio, M. Formation of the radio jet in M87 at 100 Schwarzschild radii from the central black hole. *Nature* **401**, 891–892 (1999).
19. Daly, R. D. & Marscher, A. P. The gas dynamics of compact relativistic jets. *Astrophys. J.* **334**, 539–551 (1988).
20. Fender, R. P. et al. MERLIN observations of relativistic ejections from GRS 1915+105. *Mon. Not. R. Astron. Soc.* **304**, 865–876 (1999).

21. Shapiro, S. I. & Teukolsky, S. A. *Black Holes, White Dwarfs and Neutron Stars: the Physics of Compact Objects* 362 (Wiley Interscience, New York, 1983).
22. Wandel, A., Peterson, B. M. & Malkan, M. A. Central masses and broad-line region sizes of active galactic nuclei. I. Comparing the photoionization and reverberation techniques. *Astrophys. J.* **526**, 579–591 (1999).

**Acknowledgements**

We gratefully acknowledge partial support for this research from the US National Science Foundation (NSF), NASA, the Fulbright Commission for collaboration between Spain and the USA, and the Spanish Dirección General de Investigación Científica Técnica. The VLBA is an instrument of the National Radio Astronomy Observatory, a facility of the NSF operated under cooperative agreement by Associated Universities Inc. The University of Michigan Radio Astronomy Observatory was funded in part by the NSF and by the University of Michigan Department of Astronomy.

**Competing interests statement**

The authors declare that they have no competing financial interests.

Correspondence and requests for materials should be addressed to A.P.M. (e-mail: marscher@bu.edu).

.....  
**Coherence–incoherence and dimensional crossover in layered strongly correlated metals**

**T. Valla\*, P. D. Johnson\*, Z. Yusof†, B. Wells†, Q. Li‡, S. M. Loureiro§, R. J. Cava§, M. Mikami||, Y. Mori||, M. Yoshimura|| & T. Sasaki||**

\* *Physics Department, ‡ Material Sciences Department, Brookhaven National Laboratory, Upton, New York 11973, USA*

† *Department of Physics, University of Connecticut, 2152 Hillside Road U-46, Storrs, Connecticut 06269, USA*

§ *Department of Chemistry and Princeton Materials Institute, Princeton University, Princeton, New Jersey 08540, USA*

|| *Department of Electrical Engineering, Osaka University, 2-1 Yamada-oka, Suita-shi, Osaka, 565-0871 Japan*

The properties of an interacting electron system depend on the electron correlations and the effective dimensionality. For example, Coulomb repulsion between electrons may inhibit, or completely block, conduction by intersite electron hopping, thereby determining whether a material is a metal or an insulator<sup>1</sup>. Furthermore, correlation effects increase as the number of effective dimensions decreases; in three-dimensional systems, the low-energy electronic states behave as quasiparticles, whereas in one-dimensional systems, even weak interactions break the quasiparticles into collective excitations<sup>2</sup>. Dimensionality is particularly important for exotic low-dimensional materials where one- or two-dimensional building blocks are loosely connected into a three-dimensional whole. Here we examine two such layered metallic systems with angle-resolved photoemission spectroscopy and electronic transport measurements, and we find a crossover in the number of effective dimensions—from two to three—with decreasing temperature. This is apparent from the observation that, in the direction perpendicular to the layers, the materials have an insulating character at high temperatures but become metal-like at low temperatures, whereas transport within the layers remains metallic over the whole temperature range. We propose that this change in effective dimensionality correlates with the presence of coherent quasiparticles within the layers.

Crossover in interlayer transport has been detected in layered metals such as Sr<sub>2</sub>RuO<sub>4</sub> (ref. 3) and NaCo<sub>2</sub>O<sub>4</sub> (ref. 4), and more recently in (Bi<sub>1-x</sub>Pb<sub>x</sub>)<sub>2</sub>M<sub>3</sub>Co<sub>2</sub>O<sub>7</sub>, (where M is Ba or Sr)<sup>5,6</sup>. The layers appear ‘isolated’ at high temperatures, but become connected at low

temperatures to give a three-dimensional (3D) system. A similar crossover is observed in the quasi-one-dimensional (1D) Bechgaard salt  $(\text{TMTSF})_2\text{PF}_6$  in the least-conductive direction<sup>7</sup>. The crossover temperature,  $T_M$ , is typically between 90 and 200 K. The low-temperature phase (temperature  $T \ll T_M$ ) is 3D-like in the sense that the resistivity has nearly the same temperature dependence in all three directions.

The transport in the  $c$ -axis direction (perpendicular to the layers) of an anisotropic layered system may be coherent or incoherent. In a system showing coherent transport, the electronic states are well described in terms of the dispersing 3D momentum states in the usual band formulation. The conductivity is determined by the scattering rate  $\Gamma = 1/\tau$  (where  $\tau$  is the quasiparticle lifetime) and the Fermi velocity in that direction. The system may be anisotropic, but with a nearly temperature-independent anisotropy ratio, that is,  $\rho_c(T) \propto \rho_{ab}(T) \propto \Gamma(T)$ , where  $\rho_{ab}$  and  $\rho_c$  are the in-plane and interlayer resistivities, respectively. In the case of incoherent transport, when the quasiparticle scattering rate is much greater than the effective interlayer hopping, the interlayer tunnelling events are uncorrelated. Formally, this means that the electrons are scattered many times between successive tunnelling events and the perpendicular momentum,  $k_z$ , is not a good quantum number. The conductivity,  $\sigma_c$ , is then proportional to the tunnelling rate between two adjacent layers, and assuming that the intralayer momentum is conserved in a tunnelling event<sup>8,9</sup>:

$$\sigma_c(T, \omega = 0) \propto \int \frac{d^2k}{(2\pi)^2} t_{\perp}(k)^2 G_R(k, \omega) G_A(k, \omega) \frac{\partial f(\omega)}{\partial \omega} \quad (1)$$

where  $G_{R,A}$  is the retarded or advanced in-plane Green's function near the Fermi level ( $\omega = 0$ ), where  $\omega$  is the binding energy,  $t_{\perp}(k)$  is the interplane hopping and  $f$  is the Fermi distribution. In the quasiparticle picture, the Green's functions have a coherent component  $\sim Z/(\omega - \varepsilon_k - i\Gamma)$ , where  $Z$  is the quasiparticle renormalization factor and  $\varepsilon_k$  is the renormalized quasiparticle energy. This results in the interlayer transport (equation (1)) having the same temperature dependence as the in-plane transport, dictated by

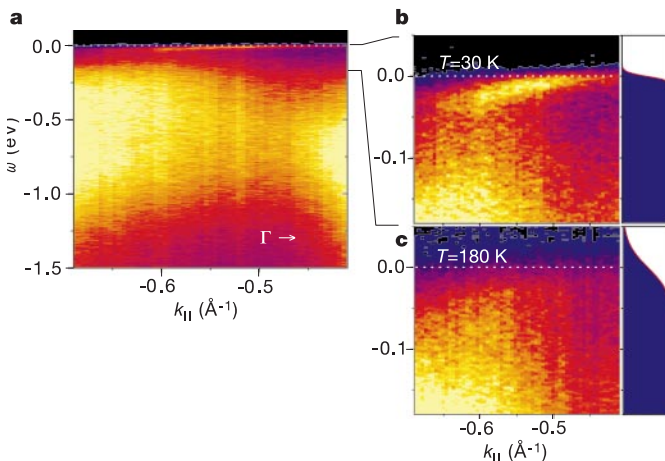


**Figure 1** Angle-resolved photoelectron spectra of  $(\text{Bi}_{0.5}\text{Pb}_{0.5})_2\text{Ba}_3\text{Co}_2\text{O}_y$ . **a**, The contour plot of the ARPES intensity along the  $(0,0)$  to  $(\pi,\pi)$  line at  $T = 30$  K. The arrow indicates the direction to the zone centre  $\bar{\Gamma}$ . Changes in the low-energy region with temperature: the 30 K **(b)** and 180 K **(c)** contour spectra (left) are plotted on the same scale with the corresponding Fermi distributions (right). The spectra were taken with a Scienta SES200 hemispherical analyser with an angular resolution of  $\pm 0.1^\circ$  or better and an energy resolution of the order of 10 meV. Photons of 15.4 eV, provided by a normal incidence monochromator based at the NLSL, were used for the excitation. Samples, grown as described in ref. 5, were mounted on a liquid He cryostat, and cleaved *in situ* in the ultrahigh-vacuum chamber with base pressure  $(2-3) \times 10^{-9}$  Pa.

$\Gamma(T)$ . The crossover behaviour that we report here therefore suggests that the quasiparticle picture is inappropriate above  $T_M$ , where conductivities are uncoupled<sup>8</sup>.

Angle-resolved photoelectron spectroscopy (ARPES) is an ideal experimental probe for testing the character of excitations. It measures directly the same single-particle spectral function  $A(k, \omega) \propto \text{Im} G(k, \omega)$  that enters the transport equation (1). However, in contrast to transport probes, ARPES is  $k$ -resolving and able to probe deeper states that may contribute to the transport only at higher temperatures,  $k_B T \approx \omega$ . Applying ARPES studies to these materials, we find that the crossover observed in transport strongly correlates with changes observed in the spectral function.

In Fig. 1 we show the photoemission intensity recorded from  $(\text{Bi}_{0.5}\text{Pb}_{0.5})_2\text{Ba}_3\text{Co}_2\text{O}_y$  in the  $(0,0)$  to  $(\pi,\pi)$  direction of the Brillouin zone. This material is a non-superconducting relative of the double-layer copper oxide superconductor  $\text{Bi}_2\text{Sr}_2\text{CaCu}_2\text{O}_{8+\delta}$ , where the Cu–O planes are substituted by Co–O. Resistivity measurements on samples from the same batch (Fig. 2b) give metallic  $\rho_{ab}$  while  $\rho_c$  shows a crossover at  $T_M \approx 200$  K. The anisotropy  $\rho_c/\rho_{ab}$  increases with decreasing temperature, saturating below  $\sim 150$  K at a value of about  $7 \times 10^3$ .

The wide-range, low-temperature spectrum (Fig. 1a) shows a broad ( $\sim 0.8$  eV full-width at half-maximum, FWHM) hump, centred at  $\sim 0.6$  eV, and a sharp state close to the Fermi level with a dip in between. The sharp peak disperses with parallel momentum,  $k_{\parallel}$ , and crosses the Fermi level with a small velocity  $V_F \approx 160$  meVÅ (note that this is one of the smallest Fermi velocities measured in ARPES), as visible in the expanded low-energy region of the contour spectrum (Fig. 1b). Our detailed studies indicate that this observation does not depend significantly on the in-plane azimuth. The sharp state forms a large, nearly cylindrical (Fermi wavevector,  $k_F \approx 0.5 \text{ \AA}^{-1}$ ), Fermi surface centred at the  $\Gamma$ -point, which remains ungapped down to the lowest measured temperature, in accord with the metallic character of Co–O planes. The state is well defined only at low temperatures and only within the range of  $\sim 40$ – $50$  meV from the Fermi level. At higher temperatures, when

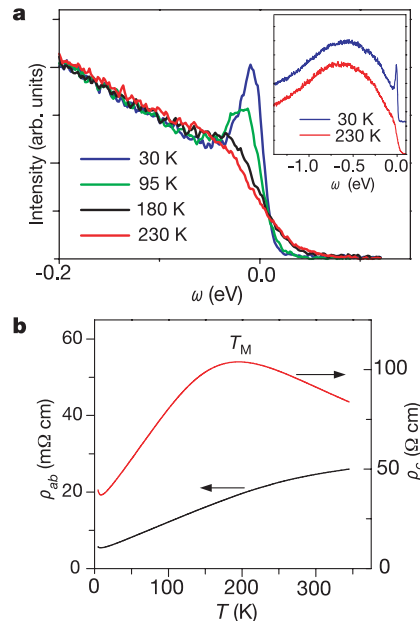


**Figure 2** Correlation between the ARPES and transport in  $(\text{Bi}_{0.5}\text{Pb}_{0.5})_2\text{Ba}_3\text{Co}_2\text{O}_y$ . **a**, The changes in energy distribution curves (vertical cross-sections of the ARPES data shown in Fig. 1) (for  $k = k_F$ ) with temperature. The inset shows the wide-range energy distribution curves. **b**, Transport data. The in-plane and the out-of-plane resistivities are measured on a sample from the same batch with a conventional four-probe technique.

$k_B T$  becomes comparable to that energy scale, the state loses coherence and the sharp peak diminishes. This is illustrated in panels Fig. 1b and c, where the spectral function is plotted on the same scale with the Fermi distribution for two given temperatures. With increasing temperature the spectrum loses its fine structure near the Fermi level. In Fig. 2 we show the temperature development of the spectral function in more detail, and correlate it with the crossover in transport. The energy distribution curves for  $k \approx k_F$  are shown for several temperatures. The sharp peak both loses intensity and broadens with temperature, with the final result that between 180 K and 230 K the spectral function that was locally peaked at  $\omega = 0$  at low temperature becomes a monotonically increasing function of energy at higher temperatures. The low-energy structure is lost, and only the broad hump characterizes the spectrum. These changes in the spectral function correlate with  $T_M$  ( $\approx 200$  K) in  $c$ -axis resistivity.

The second system that we studied was  $\text{NaCo}_2\text{O}_4$ . This material crystallizes in a layered hexagonal structure with a triangular Co lattice, octahedrally coordinated with O above and below the Co sheets. The Na ions are in the planes between the  $\text{CoO}_2$  layers. The transport properties show many peculiarities<sup>4</sup>, including a  $c$ -axis crossover at  $T_M \approx 180$  K (Fig. 3c). This system is a much better conductor than the previous one, with  $\rho_{ab} \approx 300 \mu\Omega \text{ cm}$  and an anisotropy of  $\sim 40$  at room temperature. The anisotropy increases at lower temperatures and saturates below  $\sim 120$  K at a value of  $\sim 150$ .

The spectral function of  $\text{NaCo}_2\text{O}_4$ , shown in Fig. 3, shares common features with the previous system: a broad hump at high binding energy ( $\sim 1.2$  eV FWHM) and a sharp feature that crosses the Fermi level. At high temperatures, the sharp state again disappears and the low-energy part of the spectrum is a smooth, increasing function of energy. This transformation in the spectrum again correlates with the crossover in resistivity.

When the coherent quasiparticles form in the plane (in both materials), the  $c$ -axis transport becomes metallic and the system

behaves as an anisotropic 3D metal. It is not clear, however, whether the in-plane coherence is a consequence or the cause of the dimensional crossover. One possibility is that the coherence occurs and the third dimension develops when the temperature becomes smaller than the effective energy scale for  $c$ -axis hopping. With all three dimensions ‘visible’ ( $k_B T \ll t_i$ ,  $i = x, y, z$ ), the low-energy excitations are quasiparticles. This is in line with the reasoning characterizing quasi-1D metals, where the 1D to 3D crossover is dictated by the finite inter-chain ( $t_\perp$ ) hopping integral<sup>10</sup>. In an alternative picture, sufficiently coherent ( $\Gamma(T) \ll Zt_z$ ) quasiparticles must first be formed in the planes to induce or allow coherent  $c$ -axis transport between the planes.

The crossover from coherent to incoherent excitations and a maximum in resistivity at a finite temperature is reminiscent of Kondo behaviour in heavy-fermion systems<sup>11</sup>. The latter crossover is related to the appearance of coherent, strongly renormalized (effective mass  $m^* \approx 100\text{--}1,000m_e$ , where  $m_e$  is the bare mass) quasiparticle states below the temperature at which the  $f$ -moments order, as recently observed in a photoemission study<sup>12</sup>. The systems studied here are, on the other hand, close to a Mott–Hubbard type of metal-to-insulator transition, and in one of them,  $(\text{Bi}_{1-x}\text{Pb}_x)_2\text{Ba}_3\text{Co}_2\text{O}_y$ , the transition is experimentally realized by changing the carrier concentration by lead doping<sup>5</sup>. Recent theories of the metal-to-insulator transition<sup>13–15</sup> suggest that the same physics responsible for Kondo behaviour also shapes the physical properties near the metal-to-insulator transition. In the metallic regime, these theories predict a sharp peak in the density of states near the Fermi level, in addition to separated lower and upper Hubbard bands. The sharp peak corresponds to a strongly renormalized quasiparticle band whose effective mass diverges as the ratio of the onsite Coulomb energy to intersite hopping energy,  $U/t$ , increases to some critical value at the metal-to-insulator transition. This state is responsible for the Fermi-liquid behaviour at low temperatures. However, it disappears above some characteristic temperature, and the spectral function, controlled by the high-energy physics ( $U$ ), becomes incoherent. The transport is no longer governed by coherent quasiparticles, but by collective excitations with resistivities going well beyond the Mott–Ioffe–Regel limit into a regime where the quasiparticle mean free path would be smaller than the interatomic distances<sup>16</sup>.

Depending on the ratio  $U/t$ , the incoherent response may even acquire a form characterizing the insulating side of the metal-to-insulator transition. It is important to note that although these models capture the incoherence–coherence transition, they are isotropic and therefore inappropriate for low-dimensional systems. In anisotropic materials, the different directions may be affected differently by electronic correlations. In the case of 1D Hubbard chains, for example, a small inter-chain hopping may induce deconfinement and Luttinger (1D, incoherent physics) to Fermi liquid (3D, coherent excitations) crossover<sup>17</sup>. For layered metals, equation (1) formally means that once the coherent part of the in-plane Green’s function has disappeared ( $Z \rightarrow 0$ ),  $\rho_c(T)$  is no longer bound by the in-plane transport. In other words, if the response is governed by collective excitations instead of quasiparticles, it may take different forms in different directions.

In other systems, a similar dimensional crossover to a coherent, 3D low-temperature state may be induced by different mechanisms. For example, the copper oxide high-temperature superconductors near optimal doping have metallic planes with an insulating inter-layer resistivity, again suggesting that the normal-state transport is a collective phenomenon<sup>8</sup>. Indeed, the spectral function shows the absence of sharp quasiparticle peaks in the normal state. However, these systems become (anisotropic) 3D superconductors and the quasiparticles reappear below the superconducting transition temperature,  $T_C$ , in analogy with the dimensional crossovers discussed above. The transition goes directly from 2D-like normal state into the quasiparticle-like 3D superconducting state, and cannot be

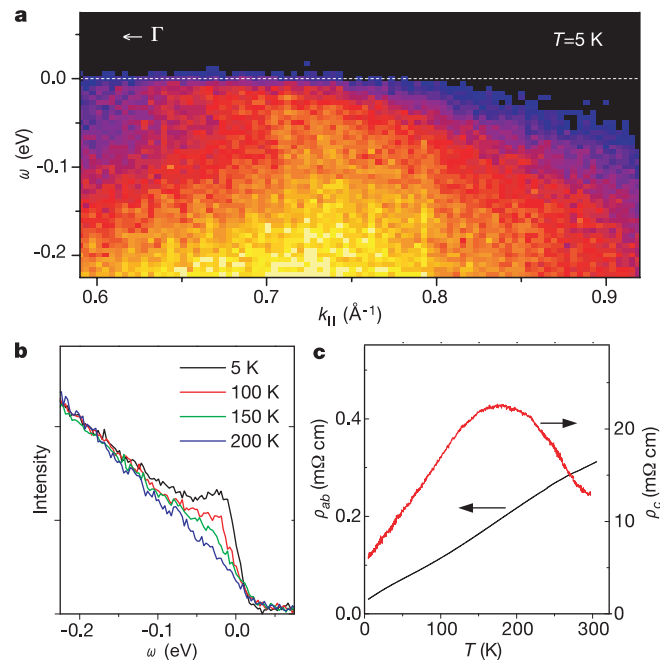


**Figure 3** ARPES and d.c. transport in  $\text{NaCo}_2\text{O}_4$ . **a**, Contour plot showing the ARPES intensity along the  $\Gamma\text{--}K$  line of the Brillouin zone at  $T = 5$  K. The Fermi crossing is a point on a large hole-like Fermi surface ( $k_F \approx 0.7 \text{ \AA}^{-1}$ ) centred at the  $\Gamma$ -point. The photon energy was 21.22 eV (He L radiation). The samples are flux grown. **b**, The temperature dependence of the low-energy region of energy distribution curves (for  $k = k_F$ ). **c**, The in-plane and out-of-plane resistivities, measured on a sample from the same batch.

dictated by the single-particle tunnelling. In the stripe picture, for example, the normal state is considered in terms of the 1D physics within the charge stripes and the superconducting transition is viewed as a 1D to 3D transition, induced by the inter-stripe Josephson tunnelling of Cooper pairs that already exist within the stripes in the normal state<sup>18</sup>.

In an alternative model, a different behaviour for in-plane and out-of-plane transport could occur if both the interlayer hopping  $t_{\perp}$ , and the Fermi surface in the plane are anisotropic<sup>9</sup>. Indeed, it has been shown<sup>19</sup> that in high-temperature superconductors, the scattering rate in the corners of the Brillouin zone that dominate  $c$ -axis hopping behaves differently from the scattering rate in the nodal regions<sup>20</sup> where  $t_{\perp} = 0$ . In addition, the corners of the Brillouin zone are affected by the normal-state pseudogap<sup>21</sup> for  $T_C < T < T^*$  ( $T^*$  is the pseudogap temperature) that blocks the normal-state  $c$ -axis transport. The inter-layer Josephson coupling then enables the transition into the 3D superconducting state without ever going through the 3D Fermi-liquid-like normal state. In the highly over-doped regime, the pseudogap disappears: the charges are then no longer confined to the planes<sup>22</sup> ( $\partial\rho/\partial T > 0$ ), even in the normal state. This transition into a 3D-like state, whether induced by single-particle tunnelling (normal state) or Josephson coupling (superconducting state), is accompanied by the appearance of a sharp peak in the spectral function<sup>23</sup>, an indication that the 3D state approaches the Fermi liquid regime. The crossover may also proceed via the exchange coupling  $J_{\perp}$ , leading to an (anti)ferromagnetic 3D ground state. In copper oxides in the low-doping regime, there are indications<sup>24</sup> that different mechanisms may compete in bringing the system into the 3D ground state. □

Received 19 November 2001; accepted 12 April 2002; doi:10.1038/nature00774.

1. Mott, N. F. *Metal-insulator Transitions* (Taylor & Francis, London, 1990).
2. J erome, D. & Caron, L. G. *Low-dimensional Conductors and Superconductors* (Plenum, New York, 1987).
3. Maeno, Y. *et al.* Superconductivity in a layered perovskite without copper. *Nature* **372**, 532–534 (1994).
4. Terasaki, I., Sasago, Y. & Uchinokura, K. Large thermoelectric power in NaCo<sub>2</sub>O<sub>4</sub> single crystals. *Phys. Rev. B* **56**, R12685–R12687 (1997).
5. Loureiro, S. M. *et al.* Enhancement of metallic behaviour in bismuth cobaltates through lead doping. *Phys. Rev. B* **63**, 094109-1–094109-9 (2001).
6. Tsukasaki, I. *et al.* Ferromagnetism and large negative magnetoresistance in Pb doped Bi-Sr-Co-O misfit-layer compound. Preprint cond-mat/0012395 at (<http://xxx.lanl.gov>) (2000).
7. Mihaly, G., Kezsmarki, I., Zambrosky, F. & Forro, L. Hall effect and conduction anisotropy in the organic conductor (TMTSF)<sub>2</sub>PF<sub>6</sub>. *Phys. Rev. Lett.* **84**, 2670–2673 (2000).
8. Anderson, P. W. *The Theory of Superconductivity in the High-T<sub>c</sub> Cuprates* (Princeton Univ. Press, Princeton, 1997).
9. Ioffe, L. B. & Millis, A. J. Zone-diagonal-dominated transport in high-T<sub>c</sub> cuprates. *Phys. Rev. B* **58**, 11631–11637 (1998).
10. Voit, J. One-dimensional Fermi liquids. *Rep. Prog. Phys.* **57**, 977–1116 (1994).
11. Fisk, Z. *et al.* Heavy-electron metals: New highly correlated states of matter. *Science* **239**, 33–42 (1988).
12. Reinert, F. *et al.* Temperature dependence of the Kondo resonance and its satellites in CeCu<sub>2</sub>Si<sub>2</sub>. *Phys. Rev. Lett.* **87**, 106401-1–106401-4 (2001).
13. Pruschke, T., Cox, D. L. & Jarrell, H. Hubbard model at infinite dimensions: Thermodynamic and transport properties. *Phys. Rev. B* **47**, 3553–3565 (1993).
14. Georges, A., Kotliar, G., Krauth, W. & Rozenberg, M. J. Dynamical mean-field theory of strongly correlated fermion systems and the limit of infinite dimensions. *Rev. Mod. Phys.* **68**, 13–125 (1996).
15. Merino, J. & McKenzie, R. H. Transport properties of strongly correlated metals: A dynamical mean-field approach. *Phys. Rev. B* **61**, 7996–8008 (2000).
16. Ioffe, A. F. & Regel, A. R. Non-crystalline, amorphous and liquid electronic semiconductors. *Prog. Semicond.* **4**, 237–291 (1960).
17. Biermann, S., Georges, A., Lichtenstein, A. & Gianmarchi, T. Deconfinement transition and Luttinger to Fermi liquid crossover in quasi one-dimensional systems. Preprint cond-mat/0107633 at (<http://xxx.lanl.gov>) (2001).
18. Carlson, E. W., Orgad, D., Kivelson, S. A. & Emery, V. J. Dimensional crossover in quasi-one-dimensional and high-T<sub>c</sub> superconductors. *Phys. Rev. B* **62**, 3422–3437 (2000).
19. Valla, T. *et al.* Temperature dependent scattering rates at the Fermi surface of optimally doped Bi<sub>2</sub>Sr<sub>2</sub>CaCu<sub>2</sub>O<sub>8+δ</sub>. *Phys. Rev. Lett.* **85**, 828–831 (2000).
20. Valla, T. *et al.* Evidence for quantum critical behaviour in the optimally doped cuprate Bi<sub>2</sub>Sr<sub>2</sub>CaCu<sub>2</sub>O<sub>8+δ</sub>. *Science* **285**, 2110–2113 (1999).
21. Ding, H. *et al.* Spectroscopic evidence for a pseudogap in the normal state of underdoped high-T<sub>c</sub> superconductors. *Nature* **382**, 51–54 (1996).
22. Watanabe, T., Fujii, T. & Matsuda, A. Pseudogap in Bi<sub>2</sub>Sr<sub>2</sub>CaCu<sub>2</sub>O<sub>8+δ</sub> studied by measuring anisotropic susceptibilities and out-of-plane transport. *Phys. Rev. Lett.* **84**, 5849–5852 (2000).
23. Yusoof, Z. *et al.* Quasiparticle liquid in the highly overdoped Bi<sub>2</sub>Sr<sub>2</sub>CaCu<sub>2</sub>O<sub>8+δ</sub>. Preprint cond-mat/0104367 at (<http://xxx.lanl.gov>) (2001).
24. Lavrov, A. N., Kameneva, M. Y. & Kozeeva, L. P. Normal-state resistivity anisotropy in underdoped RBa<sub>2</sub>Cu<sub>3</sub>O<sub>6+x</sub> crystals. *Phys. Rev. Lett.* **81**, 5636–5639 (1998).

Acknowledgements

We thank A. Tselik, R. Werner, S. A. Kivelson and A. V. Fedorov for discussions. The work at BNL and the National Synchrotron Light Source where the experiments were carried out was supported by the US Department of Energy. B.W. thanks the A.P. Sloan foundation for a Research Fellowship.

Competing interests statement

The authors declare that they have no competing financial interests.

Correspondence and requests for materials should be addressed to T.V. (e-mail: valla@bnl.gov).

Measurement of a confinement induced neutron phase

H. Rauch\*, H. Lemmel\*, M. Baron\*† & R. Loidl\*†

\*Atominstytut der  sterreichischen Universit ten, A-1020 Wien, Austria  
 †Institut Laue-Langevin, BP 156, F-38042 Grenoble, France

Particle physicists see neutrons as tiny massive particles with a confinement radius of about 0.7 fm and a distinct internal quark–gluon structure. In quantum mechanics, neutrons are described by wave packets whose spatial extent may become ten orders of magnitude larger than the confinement radius, and can even reach macroscopic dimensions, depending on the degree of monochromaticity. For neutrons passing through narrow slits, it has been predicted<sup>1,2</sup> that quantization of the transverse momentum component changes the longitudinal momentum component, resulting in a phase shift that should be measurable using interferometric methods<sup>3</sup>. Here we use neutron interferometry to measure the phase shift arising from lateral confinement of a neutron beam passing through a narrow slit system. The phase shift arises mainly from neutrons whose classical trajectories do not touch the walls of the slits. In this respect, the non-locality of quantum physics is apparent.

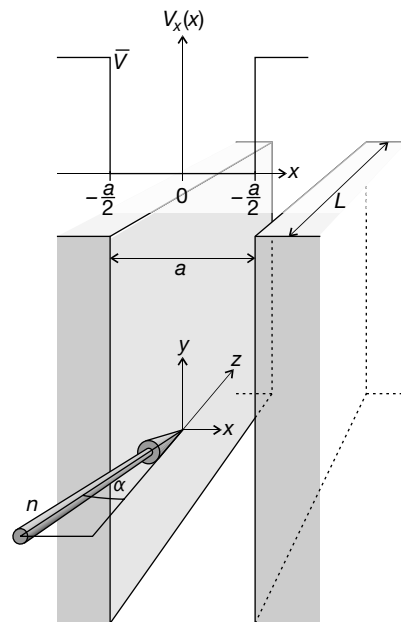


Figure 1 Sketch of the slit structure and of the related neutron–wall interaction potential. Arrow denotes neutron beam  $n$ ;  $\bar{V}$ , neutron optical potential;  $a$ , width of potential;  $L$ , length of the slit.